Weak antilocalization and disorder-enhanced electron interactions in annealed films of the phase-change compound $GeSb_2Te_4$

Nicholas P. Breznay,[1] Hanno Volker,[2] Alexander Palevski,[3] Riccardo Mazzarello,[4,5]
Aharon Kapitulnik,[1,6] and Matthias Wuttig[2,5]

[1]*Department of Applied Physics, Stanford University, Stanford, California 94305, USA*
[2]*I. Physikalisches Institut (IA), RWTH Aachen University, 52056 Aachen, Germany*
[3]*School of Physics and Astronomy, Raymond and Beverly Sackler Faculty of Exact Science, Tel-Aviv University, 69978 Tel-Aviv, Israel*
[4]*Institut für theoretische Festkörperphysik, RWTH Aachen University, 52056 Aachen, Germany*
[5]*JARA Fundamentals of Future Information Technology, RWTH Aachen, Germany*
[6]*Department of Physics, Stanford University, Stanford, California 94305, USA*

(Received 14 August 2012; revised manuscript received 3 October 2012; published 5 November 2012)

Phase-change materials can be reversibly switched between amorphous and crystalline states and often show strong contrast in the optical and electrical properties of these two phases. They are now in widespread use for optical data storage, and their fast switching and a pronounced change of resistivity upon crystallization are also very attractive for nonvolatile electronic data storage. Nevertheless, several open questions remain regarding the electronic states and charge transport in these compounds. In this work, we study electrical transport in thin metallic films of the disordered, crystalline phase-change material $GeSb_2Te_4$. We observe weak antilocalization and disorder-enhanced Coulomb interaction effects at low temperatures, and separate the contributions of these two phenomena to the temperature dependence of the resistivity, Hall effect, and magnetoresistance. Strong spin-orbit scattering causes positive magnetoresistance at all temperatures, and a careful analysis of the low-field magnetoresistance allows us to extract the temperature-dependent electron dephasing rate and study other scattering phenomena. We find electron dephasing due to inelastic electron-phonon scattering at higher temperatures, electron-electron scattering dephasing at intermediate temperatures, and a crossover to weak temperature dependence below 1 K.

DOI: 10.1103/PhysRevB.86.205302 PACS number(s): 72.15.Rn, 73.23.−b, 75.47.Np

I. INTRODUCTION

Phase-change materials such as $Ge_2Sb_2Te_5$ or $GeSb_2Te_4$ can be rapidly and reversibly switched between the amorphous and crystalline states. This phase transformation is accompanied by a significant change of optical properties, which is exploited in rewritable optical data storage.[1] Phase-change materials are also attractive for nonvolatile electronic memories, where a pronounced change of resistance[2] and fast electrical switching[3,4] are advantageous. At present, there are two challenges for commercial application of phase-change materials in electronic memories, and both are related to their electrical transport properties. First, the change of resistivity of the amorphous phase with time ("drift") is a disadvantage if multilevel storage concepts are to be realized. And second, the resistivity of the crystalline state in phase-change materials is often low, so that high currents must be applied to heat the crystalline film to the melting point and, subsequently, to bring the material to the amorphous state. To identify phase-change materials with a higher resistivity in the crystalline state, an in-depth understanding of charge transport is a prerequisite. Recent transport studies[5] have revealed a disorder-tuned metal-insulator transition in films of crystalline GeSbTe (GST) compounds. In this work, it was shown that annealing of crystalline films to progressively higher temperatures is accompanied by a change from a negative temperature coefficient of resistivity (TCR) at low annealing temperature, to a positive TCR at higher annealing temperature. This transition from an insulating to a metallic state is caused by a distinct increase of order upon annealing, and such an increase should have a pronounced impact on the low-temperature resistance. In addition, a prominent change of the magnetoresistance at very low temperature is expected upon tuning the order, i.e., upon annealing of the samples. To investigate these predictions, we have studied the low-temperature electrical transport properties of thin, quasi-two-dimensional (2D) films.

Studies of electrical transport in low-dimensional disordered conductors have revealed several quantum phenomena that can appear at low temperature, including weak localization and antilocalization quantum interference (QI) and many-body disorder-enhanced electron-electron Coulomb interaction (EEI) effects.[6] The contributions of these two effects to the temperature dependence of the resistivity, Hall effect, and magnetoresistance (MR) can be used to determine scattering mechanisms and other materials properties.[7] In 2D films, these contributions are logarithmic in temperature and have nontrivial dependences on the magnetic field. MR measurements in both perpendicular and parallel field geometries are useful for resolving these contributions, since orbital QI effects are sensitive to field orientation and can be suppressed in an applied magnetic field, while the EEI effects are isotropic and, generally, much less sensitive to the magnetic field. These techniques are well established[7] but continue to be useful in the study of electrical transport in a variety of systems, including graphene,[8] unusual oxide heterointerface structures,[9,10] and topological insulators.[11,12]

There have been few experimental studies of low-temperature transport in phase-change materials and none investigating disorder-induced quantum effects in quasi-2D films, despite considerable theoretical and practical interest in such results. Along with the recent studies of metal-insulator

transition in 100-nm-thick films,[5] there have been limited investigations of the longitudinal and Hall resistances in GST materials,[13] and of weak localization in the related compound GeMnTe.[14] Certain structures of GeSbTe are predicted to be topological insulators,[15] and considerable study has already been devoted to the related topological insulator compounds Bi_2Te_3, Bi_2Se_3, and Sb_2Te_3.[11,12]

In this paper, we report the first study of disorder-induced quantum corrections, including weak antilocalization (WAL) and enhanced EEI in thin quasi-2D GST films. At high temperatures, we observe a classical parabolic magnetoresistance and a large temperature independent contribution to the Drude resistivity. This contribution comes from static disorder and decreases monotonically with increasing annealing temperature. This large disorder gives rise to a short electronic mean-free path indicative of diffusive electronic conduction. At low temperatures ($<$20 K), we find a resistance minimum followed by a small upturn in the resistance that is proportional to $\ln(T)$ as the temperature continues to decrease. The low temperature MR is positive everywhere and shows a sharp cusp that develops below 20 K, suggesting WAL arising from diffusive carrier transport in the presence of strong spin-orbit scattering. At high fields, we are able to recover the EEI contribution to both the resistivity and the Hall effect. Finally, we analyze the MR measurements using established localization theories and determine contributions to electronic scattering. In future studies, we also intend to investigate systematic changes of QI and EEI effects upon the transition from the metallic (weakly localized) to the insulating (strongly localized) state. The data and conclusions presented in this manuscript should help to understand the relationship between structural and electronic properties,[16] recently reported high-temperature magnetoresistive effects,[17] and the role of atomic vacancies in electronic properties.[18]

Our paper is organized as follows. In Sec. II, we review the experimental parameters for our GST films, and in Sec. III, discuss the film dimensionality. Section IV contains an analysis of the low-temperature resistance and Hall effect anomaly resulting from QI and EEI effects. Section V presents the measurements and analysis of the low-temperature MR in perpendicular and parallel fields, and Sec. VI contains a detailed discussion of the dominant scattering phenomena determined from the MR measurements. Finally, Sec. VII summarizes our results and suggests open questions that may be of interest for future study.

II. EXPERIMENT AND SAMPLE CHARACTERIZATION

Films of $GeSb_2Te_4$ with thicknesses of 7.5 and 14 nm were deposited by sputtering onto Si substrates using stoichiometric GST targets and capped with a 7-nm ZnS-SiO_2 layer (with a composition ratio of ZnS:SiO_2 equal to 80%:20%). The film thicknesses d were controlled by adjusting the sputter time as confirmed using x-ray reflectivity techniques. Films were annealed for 30 minutes in pure argon gas flow at temperatures of 275 °C (samples 1 and 3) and 300 °C (sample 2); 100-nm-thick samples prepared identically were found to be in the hexagonal crystal phase.[5] After annealing, Hall-bar devices were patterned using conventional photolithography and Ar-ion milling techniques, with Ti/Au pads for electrical contact. The active area of the devices was 200 × 100 μm^2.

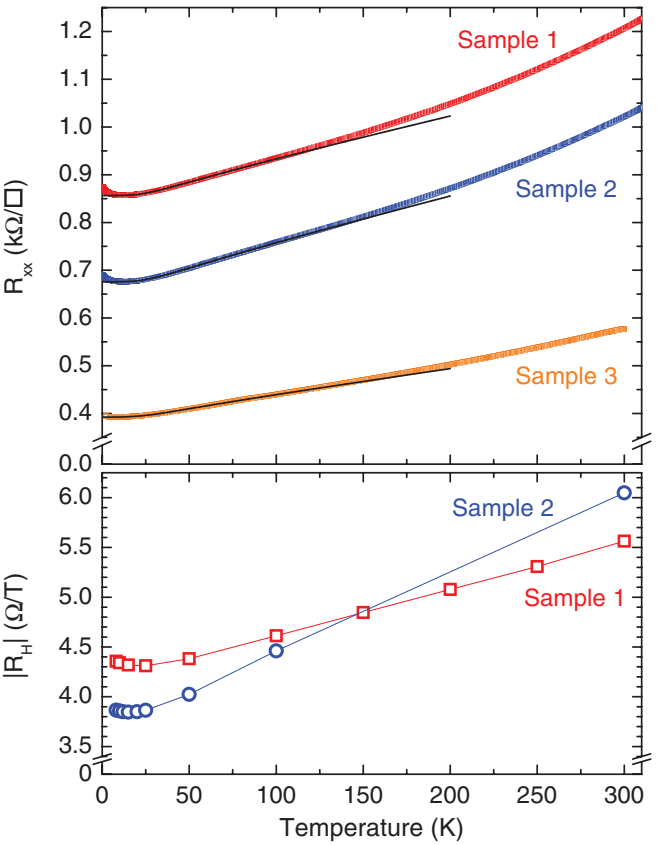

FIG. 1. (Color online) (Top) Sheet resistance R_{xx} vs temperature for three $GeSb_2Te_4$ samples showing metallic slope, large residual resistance R_0, and a low-temperature minimum. Also shown are fits (solid black lines) to a Bloch-Grüneisen form (see text). (Bottom) Hall coefficient R_H vs temperature for samples 1 and 2.

The longitudinal and Hall resistances were measured in several Quantum Design PPMS cryostats in applied magnetic fields of up to 9 T using standard four-point dc and low-frequency lock-in techniques. Three completely independent experimental systems were used and all gave identical results. Care was taken to ensure that resistances were measured in the Ohmic regime, especially at low temperatures ($<$1 K). Over 40 devices from the three films were fabricated and characterized at room temperature, and several for each film were further studied at low temperatures. All devices from the same film showed qualitatively identical behavior and only minor variation in their resistivity, Hall coefficient, and other parameters. All experimental data and formulas below report resistances R_{ij} and conductances σ_{ij} in 2D (sheet) values.

Figure 1 shows the measured sheet resistance versus temperature for all samples, which exhibit a positive temperature coefficient of resistance and weakly metallic behavior with a large zero-temperature residual resistance R_0. The increase in the resistance with increasing temperature above 20 K is consistent with an increase in electron-phonon scattering; Fig. 1 shows fits to the Bloch-Grüneisen expression[19] for the phonon contribution to electronic scattering, $R(T)/R_{\min} - 1 \sim (T/\theta_D)^5$ at the lowest temperature. We find a Debye

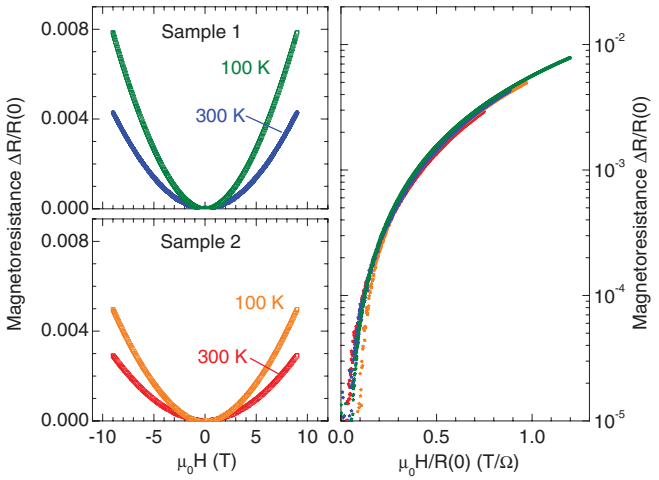

FIG. 2. (Color online) (Left) magnetoresistance for samples 1 and 2 at 300 and 100 K. (Right) Kohler diagram showing scaling of all the magnetoresistance data sets in the left panels.

temperature $\theta_D \approx 140$–150 K, consistent with independent measurements on comparable films,[20] and extract a value for the electron phonon coupling constant $\lambda_{ep} \sim 0.1$. We expect the nontrivial band structure and appearance of minority carriers in this material to yield a more complex temperature dependence of R_{xx} as T continues to increase.

The measured Hall resistance R_{xy} is linear in the applied magnetic field and is consistent with p-type carriers; we extract the Hall coefficient from high-field ($B > 2$ T) measurements of R_{xy}. The lower portion of Fig. 1 shows the Hall coefficient $R_H = R_{xy}/B$ as a function of temperature for samples 1 and 2. Multiband effects[13] should lead to a temperature dependence of R_H at high T, but we expect no temperature dependence of the carrier density in the $T = 0$ limit for such a degenerately doped semiconductor. However, R_H shows a low-temperature minimum followed by an upturn, similar to R_{xx}. We ascribe this low-temperature upturn to enhanced EEI effects as discussed in subsequent sections. The measured Hall coefficient at 15 K yields a carrier density $n \sim 2 \times 10^{20}$ cm^{-3} via $|R_H| = \frac{1}{ned}$ and a Hall angle $\tan\theta_H = R_{xy}/R_{xx} \approx 0.005$ at a field of 1 T.

The longitudinal conductance in the presence of a magnetic field $\sigma_{xx}(B)$ can be calculated from R_{xx} and R_{xy} through

$$\sigma_{xx}(B) = \frac{R_{xx}}{R_{xx}^2 + R_{xy}^2} = \frac{1}{R_{xx}}[1 + \tan(\theta_H)^2]^{-1}. \quad (1)$$

Since $\tan(\theta_H) \ll 1$, the conductance $\sigma_{xx} \approx 1/R_{xx}$ and the magnetoconductance $\Delta\sigma_{xx}(B) = \sigma_{xx}(B) - \sigma_{xx}(0) \approx 1/R_{xx}(B) - 1/R_{xx}(0)$. Below, we plot and analyze the negative magnetoconductance, $-\Delta\sigma_{xx}(B)$, which has the same sign as the MR.

Now let us consider the normal state MR. Figure 2 shows the measured MR at 300 and 100 K for samples 1 and 2, defined as

$$\frac{\Delta R}{R(0)} = \frac{R_{xx}(B) - R_{xx}(0)}{R_{xx}(0)}. \quad (2)$$

At these temperatures, the MR is small, positive, and parabolic. Kohler's rule[19] states that in a classical metal with one dominant scattering time, the MR should be a universal function of the quantity $\omega_c\tau_e$, where τ_e is the transport scattering time, the cyclotron frequency $\omega_c \equiv eB/m^*$, and m^* is the effective mass. At sufficiently low fields,

$$\frac{\Delta R}{R(0)} \sim (\omega_c\tau_e)^2, \quad (3)$$

consistent with the data presented in Fig. 2. From parabolic fits to the 300 K curve for sample 1, we derive $\tau_e \approx 1.4 \times 10^{-14}$ s and a mobility $\mu \approx 61$ cm^2/(V s), comparable to the calculated Hall mobility $\mu_{\rm Hall} \approx 36$ cm^2/(V s) and somewhat larger than that achieved in thick (100 nm) films annealed to the same temperatures.[5] For free electrons, $\omega_c\tau_e = BR_H/R_{xx}$ and so the normal state MR should be a universal function of B/R_{xx}; such scaling for samples 1 and 2 is shown in the right panel of Fig. 2, consistent with a free-electron, single scattering time picture of the classical electrical transport from 100–300 K. In our consideration of the low temperature MR below, this classical contribution was also apparent at the highest fields and was subtracted before proceeding with quantitative analysis.

Based on the measured resistivity, Hall coefficient, and MR, we calculated materials parameters including the mean-free path ℓ_e and diffusion coefficient $D_{\rm tr}$ as shown in Table I for each sample, assuming a free-electron like picture with effective mass $m^* = 0.4m_e$ and a valley degeneracy $N_v = 4$.[5]

III. SAMPLE DIMENSIONALITY

Before considering the weak localization (WL) behavior apparent in our films, let us discuss their dimensionality. A thin film can be treated as two dimensional if the thickness d is smaller than the appropriate physical length scales. However, due to the many interactions and phenomena that

TABLE I. Measured and calculated GST sample parameters. The sheet resistance R_{xx}, carrier density n, mean-free path ℓ_e, and diffusion coefficient $D_{\rm tr}$ are measured or calculated from 15 K data. (We assume the sample 3 carrier density to be equal to sample 1.) The mobility extracted from the MR $\mu_{\rm MR}$ and from the Hall effect $\mu_{\rm Hall}$ were determined using 300 K MR data. $T_{\rm min}$ is the resistance minimum temperature and d is the film thickness.

Sample	$T_{\rm anneal}$ (°C)	d (nm)	R_{xx} (kΩ/□)	n (10^{20} cm^{-3})	ℓ_e (nm)	$T_{\rm min}$ (K)	$\mu_{\rm Hall}$ (cm^2/V s)	$\mu_{\rm MR}$ (cm^2/V s)	$D_{\rm tr}$ (cm^2/s)
1	275	7.5	0.86	1.9	3.7	14	36	61	4.1
2	300	7.5	0.68	2.2	4.4	12	37	73	4.9
3	275	14.0	0.39	(1.9)	4.4	9	59	62	4.7

are relevant in this analysis, there is no single measure of our film dimensionality. The electronic mean-free path ℓ_e for the samples is ∼4 nm, less than $d = 7.5$–14 nm, and so the classical diffusive transport is three dimensional. For QI effects, the relevant length scale is the dephasing length L_ϕ, related to the phase breaking time τ_ϕ through $L_\phi = \sqrt{D\tau_\phi}$. In these samples, the dephasing is dominated by inelastic scattering, both electron-phonon scattering at high temperatures, and electron-electron scattering at lower temperatures. The rates for both of these scattering processes increase with temperature, and thus the L_ϕ decreases with temperature. At a sufficiently low temperature, there should be a crossover to 2D behavior when $L_\phi \sim d$, which (based on the analysis below) should occur at roughly 50–100 K. For EEI effects, the relevant length is the thermal diffusion length, $L_T = \sqrt{D\hbar/k_B T}$, which is equal to the film thicknesses at $T \sim 40$ K (sample 3) up to 140 K (sample 2). Thus despite being 3D with respect to classical transport, our films can be treated as 2D for QI and EEI phenomena below ∼40 K. We restrict our analysis to this quasi-2D limit.

The characteristic phonon wavelength $\lambda_{\rm ph} = \hbar v_s/k_B T \sim 1$ nm at 15 K, smaller than the film thicknesses, indicating that the phonons cannot be considered two dimensional and therefore constraining the theoretical predictions for the electron-phonon scattering rates. Finally, the characteristic magnetic length $\ell_B = \sqrt{\hbar/4eB}$ is equal to the 7.5-nm thickness of samples 1 and 2 at ∼3 T and equal to the sample 3 film thickness of 14 nm at ∼1 T; at higher fields, the diffusive transport is no longer in the quasi-2D limit. We now turn to an analysis of the anomalous upturn in the resistance apparent at temperatures below 20 K.

IV. WEAK LOCALIZATION AND LN(T) RESISTANCE

A. Theoretical background

The low temperature electrical conductance σ_{xx} of a disordered metallic film in the presence of weak localization QI and EEI corrections can be written as

$$\sigma_{xx}(B,T) = \sigma_0 + \Delta\sigma^{\rm QI,EEI}(B,T), \tag{4}$$

where $\sigma_0 = \frac{ne^2\tau_e d}{m^*}$ is the (classical) Drude conductance, and the remaining term arises from disorder-induced QI and enhanced EEI effects. These corrections have been studied extensively[6] and are especially pronounced in systems of reduced dimensionality. In 2D, both effects lead to a $\ln(T)$ contribution to the conductance.

At high temperatures, when the electronic phase coherence time (τ_ϕ) is very short, the diffusive charge transport in a disordered film can be treated classically. As the temperature is decreased, electron-phonon and other inelastic scattering events (which randomize the electronic phase and thus limit τ_ϕ) are suppressed. Once τ_ϕ becomes long relative to the elastic scattering time τ_e, QI effects appear. WL results in an upturn in the resistance at low temperature arising from constructive interference of self-intersecting time-reversal-symmetric trajectories. WAL occurs when spin-orbit scattering is strong, and results in a decrease in the resistance. The WL correction, $\Delta\sigma(T) \sim \ln(\tau_\phi/\tau_e)$, is sensitive to the dephasing time since only trajectories that are coherent within this timescale can interfere. The characteristic amplitude of these effects is $G_0 \equiv \frac{e^2}{2\pi^2\hbar}$, and if the inelastic scattering rate has a power-law dependence on the temperature, $\tau_\phi^{-1} \sim T^p$, then the WL correction is proportional to $\ln(T)$:[21]

$$\Delta\sigma^{\rm QI}(T) = G_0 pt N_v \eta \ln(T/T_0). \tag{5}$$

Here, T_0 is a reference temperature, N_v is the number of degenerate valleys, η is related to the strength of intervalley scattering, and the prefactor $N_v\eta$ is of order unity. ($N_v\eta \to 1$ when intervalley scattering is strong, and $N_v\eta \to N_v$ when intervalley scattering is weak.) Finally, t relates to the strength of spin-orbit scattering, $t = 1$ in the weak spin-orbit scattering (WL) limit ($\tau_{so}^{-1} \ll \tau_\phi^{-1}$), and $t = -\frac{1}{2}$ in the opposite (WAL) limit ($\tau_{\rm so}^{-1} \gg \tau_\phi^{-1}$).

The EEI correction to the conductance[6,22] also shows a $\ln(T)$ dependence,

$$\Delta\sigma^{\rm EEI}(T) = G_0\left(1 - \tfrac{3}{4}F_\sigma\right)\ln(T/T_0), \tag{6}$$

where F_σ is a 2D effective screening parameter and in the limit of strong spin-orbit scattering $F_\sigma \to 0$.[22,23] Assuming that the QI and EEI effects are additive, the total zero-field contribution to the conductance is

$$\Delta\sigma(T) = G_0 A \ln(T/T_0), \tag{7}$$

where the prefactor A is given by

$$A = N_v\eta tp + 1 - \tfrac{3}{4}F_\sigma. \tag{8}$$

Modest applied magnetic fields suppress the WL correction but not the EEI term, so we now consider our measurements of the conductance in zero and applied fields as a function of temperature.

B. Temperature dependence of the conductance

Figure 3 shows the conductance versus temperature for each sample. Also shown are linear fits in the temperature range 0.7 to 5 K, where the data are approximately linear in $\ln(T)$, with slopes $A \sim 0.7$. As shown in Eq. (8), these slopes contain contributions from QI and EEI effects. Measuring this slope in applied magnetic fields allows separation of the two, since the QI effect can be suppressed with a moderate field, while the EEI contribution contributes only weakly to the MR and cannot be suppressed. The lower portion of Fig. 3 shows the conductance in applied fields ranging from 0 up to 200 mT for sample 1, along with linear fits to the low-temperature data (dashed lines). The resulting logarithmic slope A for each fits (along with additional fits at higher fields, not shown on the plot) are shown in the inset.

The slope of the longitudinal conductance is $A_{\rm Low} \sim 0.70$ in zero field, and saturates to $A_{\rm Hi} \sim 1.2$ at fields of roughly 0.5 T or more. Based on our analysis of MR measurements (see discussion below), we know that the characteristic dephasing field B_ϕ for suppression of the QI correction is less than 0.1 T throughout this temperature range; thus 0.5 T should

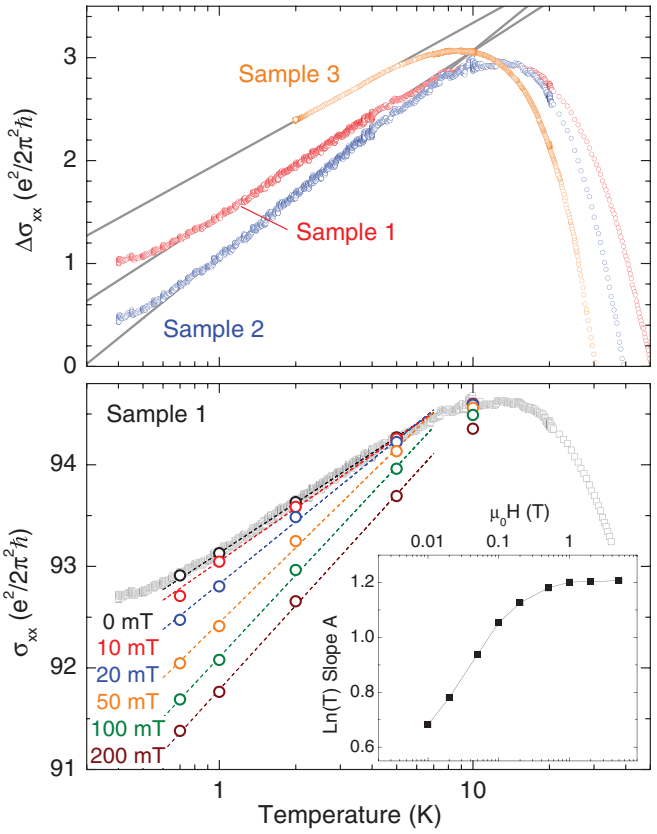

FIG. 3. (Color online) (Top) Relative change in conductance vs temperature for all three GST samples along with linear fits in $\ln(T)$; the curves have been displaced vertically for clarity. (Bottom) Conductance of sample 1 in zero field and applied magnetic fields of 10, 20, 50, 100, and 200 mT. (Inset) Slope of $\ln(T)$ fits for sample 1 as a function of applied magnetic field on double logarithmic scales, showing saturation at fields above ~0.5 T.

be sufficient to suppress the QI localization effect. With the QI conductance correction slope $A^{\rm QI} = A_{\rm Low} - A_{\rm Hi} \approx -0.5$, the remainder should be due to EEI: $A^{\rm EEI} = A_{\rm Hi} \approx 1.2$. The value for $A^{\rm QI}$ is consistent with strong intervalley scattering ($N_v\eta \to 1$), $t = -1/2$ (the strong spin-orbit scattering, or WAL, limit), and $p \approx 1$ as expected for electron-electron scattering dominated dephasing (see discussion below). In the limit of very strong screening and strong spin-orbit scattering $F_\sigma \to 0$, the EEI contribution $A^{\rm EEI}$ should be 1. Our value of 1.2 indicates either that the parameter F_σ is negative or that there is an additional $\ln(T)$ contribution to the conductance appearing at low temperature beyond those considered here.

Table II shows the collected results from the analysis of the zero-field and in-field resistance versus temperature measurements. We comment that the observed EEI effects seen in these metallic samples showing WL behavior does not contradict the observations of Siegrist *et al.*,[5] who highlighted the importance of disorder relative to electron interaction effects to explain the MIT in thicker films of this material. Recent studies[11] of WAL in the topological insualtor Bi_2Se_3 have also found evidence for EEI effects in their analyses of magnetotransport measurements. Since the QI and EEI corrections are expected to contribute to R_H in distinct ways,

TABLE II. Weak localization analysis of resistance vs temperature data for the three samples. The coefficient A is determined from zero-field data, and the EEI prefactor $1 - \frac{3}{4}F_\sigma$ from data measured in applied fields larger than ~0.5 T. The QI prefactor $tpN_v\eta$ is the difference between these values.

Parameter	Sample 1	Sample 2	Sample 3
A	0.71	0.69	0.56
$A^{\rm EEI} = 1 - \frac{3}{4}F_\sigma$	1.22	1.18	1.15
$A^{\rm QI} = tpN_v\eta$	−0.51	−0.49	−0.59

further consideration of temperature dependent Hall effect data can supplement the above analysis.

C. Temperature dependence of the Hall effect

Figure 4 shows the Hall coefficient R_H, along with the longitudinal resistance measured in zero field, $R_{xx}(0)$, and 5 T, $R_{xx}(5\ {\rm T})$, all as a function of temperature for sample 1. The three curves have been scaled by the resistance minimum value $R_{\rm min}$; plotted is

$$\frac{\Delta R_i}{R_{i,\rm min}} \equiv \frac{R_i(T) - R_{i,\rm min}}{R_{i,\rm min}}, \tag{9}$$

where R_i is either $R_{xx}(0)$, $R_{xx}(5T)$, or R_H. The behavior of R_H is similar to that analyzed for R_{xx} in the previous section; R_H shows a minimum between 10 and 20 K followed by an upturn that is linear in $\ln(T)$. Also shown in Fig. 4 are linear fits to the low temperature $\ln(T)$ portion of each data set; the slopes S_i are listed in the inset.

Both the QI and EEI localization effects[24] contribute to the diagonal conductance σ_{xx} as described in Eq. (4), while only the QI effect contributes to the Hall conductance σ_{xy},

$$\sigma_{xy} = \sigma_{xy}^D + \Delta\sigma_{xy}^{\rm QI}, \tag{10}$$

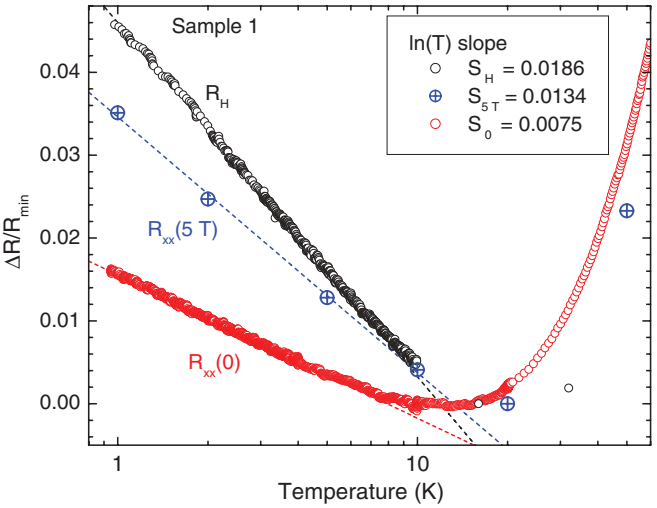

FIG. 4. (Color online) Relative change in the Hall coefficient R_H and longitudinal resistance at zero field [$R_{xx}(0)$] and 5 T [$R_{xx}(5\ {\rm T})$] vs temperature for sample 1. Also shown are linear fits (dashed lines) to the low-temperature region of each proportional to $\ln(T)$. Values for the slope S of the three linear fits are listed in the inset.

where here σ_{xy}^{D} is the classical Drude contribution to the Hall effect. When inverting the conductivity tensor σ_{ij}, if only QI effects are present, then (to lowest order) there is no correction to R_H, while if only EEI effects are present, then the correction to the Hall coefficient R_H is twice that to the longitudinal resistance:

$$\left(\frac{\Delta R_H}{R_H}\right)^{\mathrm{EEI}} = 2\left(\frac{\Delta R_{xx}}{R_{xx}}\right). \tag{11}$$

Finally, if both QI and EEI corrections are present, then the Hall coefficient correction will include both QI and EEI terms:[23]

$$\left(\frac{\Delta R_H}{R_H}\right) = \frac{2\Delta\sigma^{\mathrm{EEI}}}{\Delta\sigma^{\mathrm{QI}} + \Delta\sigma^{\mathrm{EEI}}}\left(\frac{\Delta R_{xx}}{R_{xx}}\right). \tag{12}$$

Since our measurements of the Hall coefficient were performed at magnetic fields much larger than the dephasing field ($B \gg B_\phi$), we would expect this to suppress the QI term in Eq. (12) above, so that the correction to the Hall coefficient ($\Delta R_H/R_H$) should be two times the R_{xx} correction as in Eq. (11). The measured ratio $(\Delta R_H/R_H)$ / $[\Delta R_{xx}(5T)/R_{xx}(5T)] = S_H$ / S_{5T} is 1.4, close to the predicted value of 2 and confirming the presence of EEI corrections at high field. Studies of 2D electron systems in Si[25] and InZnO films[26] observed ratios in the range 1–2, recovering the theoretical prediction of 2 in the $R_{xx} \to 0$ limit.

In the low-field limit, we expect from Eq. (12) to observe $(\Delta R_H/R_H)$ / $[\Delta R_{xx}(0)/R_{xx}(0)] = 2S_{5T}/S_0 = 3.6$. The measured ratio $S_H/S_0 = 2.5$ is comparable to this value, given that the Hall coefficient measurement was performed at high field. While it is difficult to obtain precise Hall coefficient measurements in the zero-field limit, we did observe a qualitative increase in the slope S_H as $B \to 0$. This increase would give a larger value of S_H/S_0, consistent with the theoretical prediction of Eq. (12). Additional study of the field and disorder dependence of the Hall coefficient at low temperature should further inform this analysis. Having resolved QI and EEI contributions to the resistance and Hall coefficient at low T, let us now consider the WL contributions to the MR, with the final goal of understanding the scattering mechanisms that govern the electronic dephasing processes in these materials.

V. MAGNETORESISTANCE ANALYSIS

A. Perpendicular field

Figure 5 shows the measured MR for samples 1 and 2 at all temperatures, from 300 to 0.4 K. Below 50 K, the Kohler rule scaling of the MR breaks down, and a pronounced cusp near zero field appears. Perpendicular magnetic fields suppress QI effects by destroying the phase coherence of time-reversal-symmetric paths. In the case of WAL, this results in a positive MR, consistent with the data in Fig. 5 and indicating that we must consider spin-dependent scattering effects. The temperature and field dependent QI correction to the conductance, in the presence of spin-orbit and spin-flip scattering, was first described by Hikami, Larkin, and

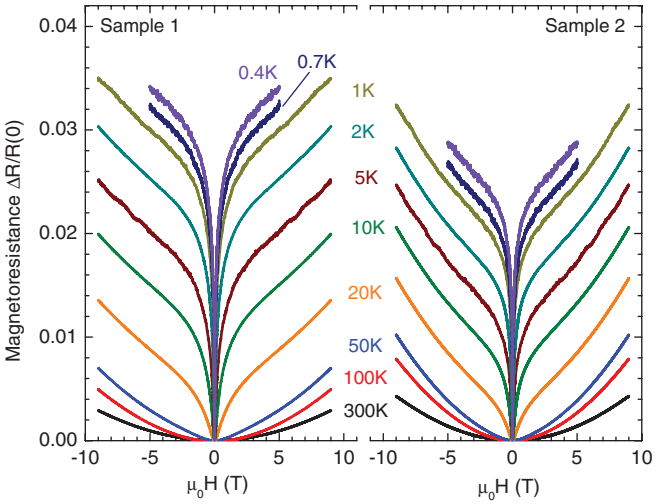

FIG. 5. (Color online) Magnetoresistance for sample 1 (left) and 2 (right) from 300 to 0.4 K; temperatures are indicated for each curve.

Nagaoka[21] (HLN),

$$\sigma_{\mathrm{QI}}(T,B) = -G_0\alpha\left[\Psi\left(\frac{B_1}{B}\right) - \frac{3}{2}\Psi\left(\frac{B_2}{B}\right) + \frac{1}{2}\Psi\left(\frac{B_3}{B}\right)\right], \tag{13}$$

where $\Psi(x) = \psi(1/2 + x)$, $\psi(x)$ is the digamma function, α is a constant of order 1, and $\mathrm{B}_{1,2,3}$ are given by

$$B_1 = B_e + B_{\mathrm{so}} + B_s, \tag{14}$$

$$B_2 = \tfrac{4}{3}B_{\mathrm{so}} + \tfrac{2}{3}B_s + B_i, \tag{15}$$

$$B_3 = 2B_s + B_i. \tag{16}$$

Here, $B_x = \frac{\hbar}{4eD\tau_x}$ is the characteristic field corresponding to spin-orbit (so), spin-flip (s), elastic (e), and inelastic (i) scattering processes. Note that the dephasing rate $\tau_\phi^{-1} = 2\tau_s^{-1} + \tau_i^{-1}$, and so we identify B_3 above as the corresponding dephasing field, $B_\phi = B_3 = 2B_s + B_i$. In the limit of moderate spin-orbit and weak spin-flip scattering, $B_e \gg B_{\mathrm{so}} \gg B_s$, we may further simplify the above expression:

$$\Delta\sigma(B) = -G_0\alpha\left[\psi\left(\frac{1}{2} + \frac{B_e}{B}\right) - \frac{3}{2}\psi\left(\frac{1}{2} + \frac{\frac{4}{3}B_{\mathrm{so}} + B_\phi}{B}\right) + \frac{1}{2}\psi\left(\frac{1}{2} + \frac{B_\phi}{B}\right)\right]. \tag{17}$$

Figure 6 shows the negative magnetoconductance determined for sample 3 at fields comparable to B_ϕ; note that the magnetic field is plotted on a logarithmic scale, and the curves are offset vertically. The magnitude of the magnetoconductance is of order of the WL prefactor G_0. Figure 7 shows the negative magnetoconductance up to fields well above B_ϕ for sample 1. Note that we have subtracted the (classical) parabolic contribution to the MR discussed in Sec. II above. At the highest fields measured, the sign of the MR remains positive though appearing to saturate.

To reliably determine the characteristic fields appearing in Eq. (17), we first extract B_ϕ from the low-field magnetoconductance, and then B_{so} and α using the remaining

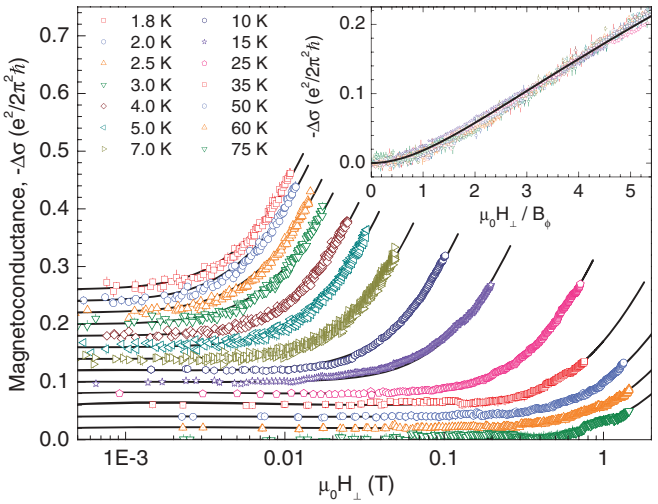

FIG. 6. (Color online) Negative magnetoconductance $-\Delta\sigma_{xx}$ for sample 3 in perpendicular applied fields $\mu_0 H \sim B_\phi$ at temperatures from 75–1.8 K, plotted on a semilogarithmic scale. The continuous curves show single parameter fits to the theory of Hikami, Larkin, and Nagaoka[21] (HLN). The data and curves have been offset vertically for clarity. (Inset) All magnetoconductance data from the main panel collapse to the theoretical HLN prediction (continuous curve) when plotted against $\mu_0 H/B_\phi(T)$.

high-field data. At low fields, the classical magnetoresistance is negligible, and below B_ϕ, we expect $\sim B^2$ MR behavior due to QI, since in the limit of $B \ll (B_{so}, B_e, B_\phi)$, Eq. (13) simplifies to

$$\Delta\sigma(B) = -G_0 \frac{1}{48}\left(\frac{B}{B_\phi}\right)^2. \tag{18}$$

Representative fits used to extract B_ϕ using only the low-field portion ($B < 5B_\phi$) of the magnetoconductance data are shown in Fig. 6 for sample 3. To determine the spin-orbit field, we keep B_ϕ constant from the low-field analysis and considered the full magnetic field range measured. The fits shown in Fig. 7

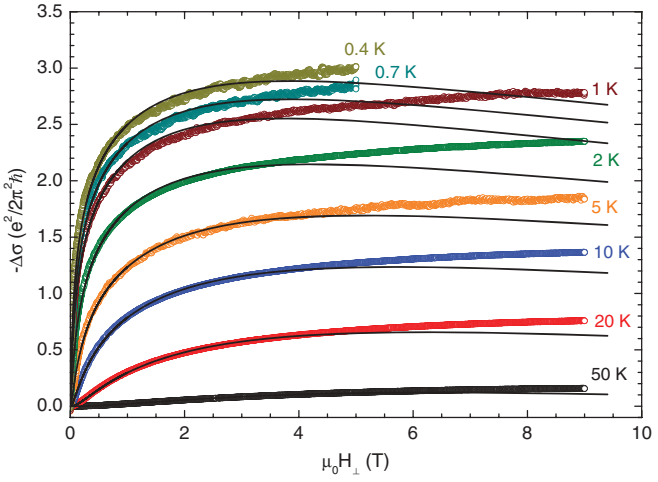

FIG. 7. (Color online) Negative magnetoconductance $-\Delta\sigma_{xx}$ vs applied perpendicular magnetic field for sample 1 at temperatures from 50 to 0.4 K, along with fits (continuous lines) to the WL theory of Hikami, Larkin, and Nagaoka as described in the text.

have only two free parameters: the spin-orbit field B_{so} and the prefactor α appearing in Eq. (17). The elastic scattering field B_e was fixed based on the estimated transport scattering time $\tau_e \approx 10^{-14}$ s, yielding $B_e \sim 10$ T. The parameters B_ϕ and B_{so} from these fits are discussed below.

Deviations in the fits shown in Fig. 7 appear at fields above ~3 T; we attribute these to the breakdown of the diffusion approximation, since they appear at $B \sim B_e/3$ and therefore are outside the region of validity for the diffusive-limit HLN theory. In addition, above this field scale the film is no longer strictly 2D, since the magnetic length $\ell_B < d$. High-field disagreement with the HLN theory is often attributed to spin-splitting or EEI contributions to the magnetoconductance. However, in the presence of strong spin-orbit scattering,[6] magnetic fields necessary to observe spin-splitting effects must satisfy $g\mu_B B \gg \hbar/\tau_{so}$, where g is the Landé g factor and μ_B is the Bohr magneton; taking $g = 2$, we estimate that fields of 30 T or higher would be required to resolve spin-splitting effects. Furthermore, both spin-splitting and EEI effects should be isotropic, and we observe no such deviations appearing in the parallel field data considered in the next section.

B. Parallel fields

When only considering orbital QI effects, a parallel magnetic field should not yield any MR with a strictly 2D film. However, as first described by Al'tshuler and Aronov[27] (AA), a nonzero film thickness will allow for electron diffusion perpendicular to a field directed parallel to the film, and therefore lead to similar suppression of QI phenomena as in the perpendicular field case. According to AA, the resulting magnetoconductance is

$$\Delta\sigma(B_{//}) = G_0 \ln\left(1 + \frac{B_{//}^2}{B_3 B_d}\right), \tag{19}$$

where $B_d = \frac{12\hbar}{ed^2}$. When including spin-flip and spin-orbit scattering, this expression becomes[28,29]

$$\Delta\sigma(B_{//}) = G_0\left[\frac{3}{2}\ln\left(1 + \frac{B_{//}^2}{B_2 B_d}\right) - \frac{1}{2}\ln\left(1 + \frac{B_{//}^2}{B_3 B_d}\right)\right]. \tag{20}$$

The magnetoconductance in parallel fields for sample 1 was also measured for a similar set of temperatures and magnetic fields; these data are plotted in Fig. 8. If the measured parallel-field MR arose from a small out-of-plane field appearing due to misalignment of the field orientation, then the data could be simply scaled to the perpendicular field results, but no such scaling is possible. While we cannot rule out the presence of a small out-of-plane contribution, the size of the measured magnetoconductance and lack of scaling indicates that this is not a significant contribution. Figure 8 also shows fits to the theory for QI contributions to the magnetoconductance in parallel field, Eq. (20), with B_ϕ and B_{so} as free parameters. The resulting values for the dephasing field B_ϕ are consistent with the perpendicular field analysis and are discussed below. In addition, the excellent agreement up to the highest magnetic fields suggests that isotropic effects, such as arising from EEI or Zeeman splitting, may be ignored in this field range.

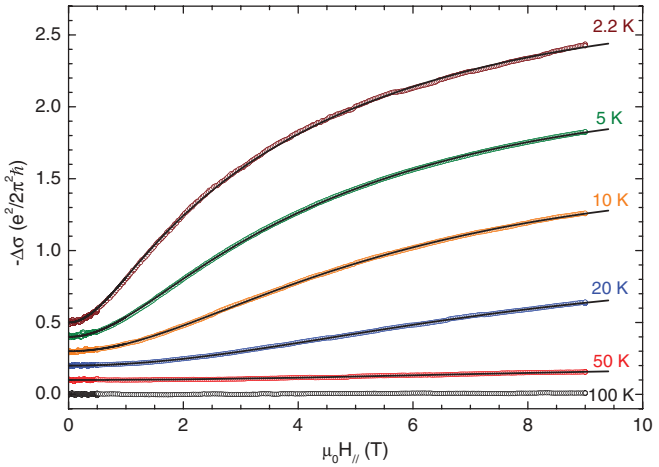

FIG. 8. (Color online) Parallel field negative magnetoconductance $-\Delta\sigma_{xx}$ for sample 1, along with fits (continuous lines) to the theory of Al'tshuler and Aronov. The curves have been vertically offset for clarity.

Figure 9 presents the characteristic fields associated with dephasing and spin-orbit scattering, extracted from fits to the 2D WL theory as described above. The dephasing field B_ϕ plotted on the lower panel shows reasonable agreement between the perpendicular and parallel field measurements for sample 1, and increases strongly with increasing temperature for all three samples. This strong temperature dependence is expected, since the field is proportional to the inelastic scattering rate which itself should increase as the temperature increases due to stronger electron-phonon and electron-electron scattering effects. We analyze this quantitatively in the next section. The spin-orbit scattering fields are roughly temperature independent, particularly in the zero-temperature limit where $B_{so} \gg B_\phi$, and appear to be consistent with

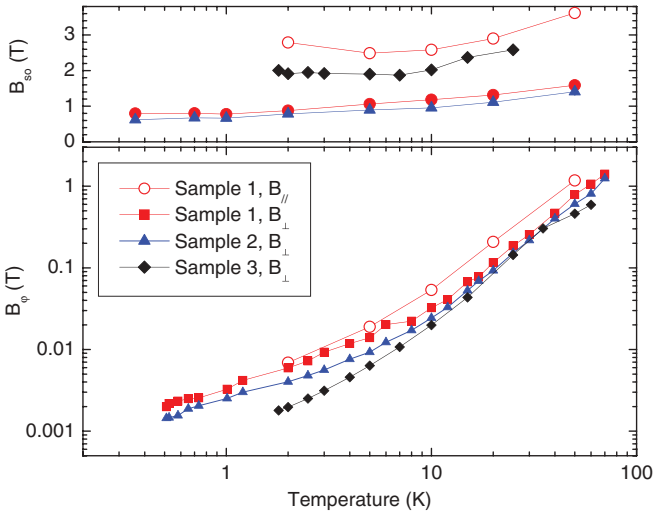

FIG. 9. (Color online) Characteristic dephasing B_ϕ and spin-orbit scattering B_{so} fields, extracted from fits to the magnetoconductance data, for all three samples in perpendicular (closed symbols) and parallel (open symbols) fields as a function of temperature. The upper panel shows B_{so} on a linear scale, while the lower panel shows the strongly temperature dependent B_ϕ on a logarithmic scale.

established theory for surface scattering in the presence of high-Z atoms.

Studies of interfacial spin-orbit scattering[30] found that when surface scattering is the dominant elastic mechanism, B_{so} can be expressed relative to the elastic scattering field B_e as $B_{so} = (\alpha_{fs} Z)^4 B_e$, where Z is the atomic number and α_{fs} is the fine structure constant. Both antimony and tellurium have large Z; assuming stoichiometric $GeSb_2Te_4$ we estimate an average atomic number $\bar{Z} \sim 49$ and therefore with $B_e \approx 10$ T would expect $B_{so} \sim 0.16$ T, somewhat smaller than the $B_{so} \sim 0.5$–2 T extracted above for the three samples. However, the scaling of the spin-orbit times for samples 1 and 2 (both 7.5 nm thick) yields $\tau_{so,\text{sample 1}}/\tau_{so,\text{sample 2}} \sim 1.19$, comparable to the ratio of elastic scattering times $\tau_{e,\text{sample 1}}/\tau_{e,\text{sample 2}} \sim 1.13$. This finding is consistent with the Elliott-Yafet[31] (EY) mechanism for spin-orbit scattering, expected to dominate in narrow-band-gap semiconductors with large valence band spin-splitting such as InSb.[32] In the degenerate case, the EY spin-orbit scattering time is given by

$$\frac{1}{\tau_{so}^{EY}} = \alpha_{EY} \frac{1}{\tau_e} \left(\frac{E_F}{E_G} \right)^2, \tag{21}$$

where E_F and E_G are the Fermi and band gap energies, and α_{EY} is related to E_G and the spin-orbit splitting.[32] Taking $\alpha_{EY} = 0.36$, we calculate $\tau_e/\tau_{so}^{EY} \sim 0.03$, while the experimentally measured ratio $B_{so}/B_e \sim 0.04$ (0.05) for sample 1 (2) is in reasonable agreement with the EY model.

The spin-orbit scattering fields are anisotropic and thickness-dependent, with $B_{so}^{\perp} \sim 0.8$ T and $B_{so}^{||} \sim 2.6$ T for sample 1, and sample 3 (which is ~2 times thicker than 1 and 2) having $B_{so}^{\perp} \sim 1.94$ T. Similar studies of WAL in strong spin-orbit materials such as Bi[33] find no such anisotropy in B_{so}, and in contrast to our results also find that the spin-orbit scattering rate decreases with increasing thickness. Further study of high-field MR in both parallel and perpendicular field may illuminate this discrepancy and inform ongoing study of spin-orbit coupling in phase-change material compounds and in related topological insulator materials such as Sb_2Te_3.

VI. SCATTERING RATES

Now, let us consider the contributions to inelastic scattering in our samples, which we may compare with the characteristic dephasing rates τ_ϕ^{-1} extracted using the MR analysis above. In addition to temperature-independent dephasing due to spin-flip scattering from magnetic impurities or other extrinsic effects,[34] the two temperature-dependent contributors to the dephasing are inelastic electron-phonon (e-p) and electron-electron (e-e) scattering. At sufficiently low temperatures, e-e scattering dephasing should dominate, since the e-p rate has a stronger temperature dependence.[35]

A. Electron-electron scattering

Al'tshuler, Aronov, and Khmelnitski (AAK)[36] and other works[35] found that for the e-e scattering rate $\tau_{i,(e-e)}^{-1}$ in the 2D limit ($L_T > d$), the following expression holds:

$$\tau_{i,(e-e)}^{-1} = \pi G_0 R_{xx} \frac{k_B T}{\hbar} \ln G, \tag{22}$$

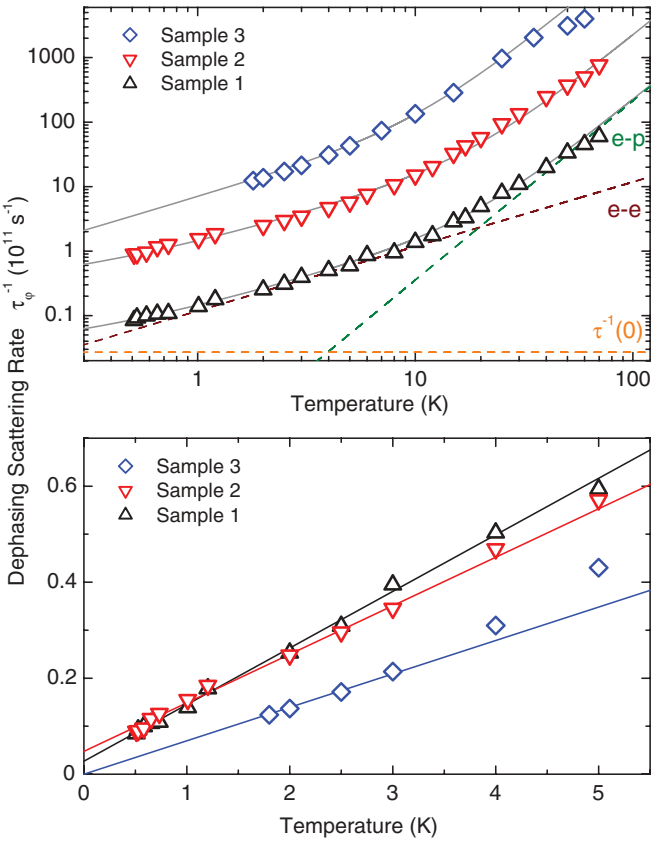

FIG. 10. (Color online) (Top) Dephasing scattering rate versus temperature on logarithmic scales for all three samples. The solid curves show fits to a theoretical model including e-p and e-e scatterings and a phenomenological T-independent dephasing rate as described in the text. The data and fits for sample 2 (3) have been multiplied by a factor of 10 (100) for clarity. The dotted curves show the separate contributions for sample 1 from T-independent dephasing, T-linear electron-electron scattering, and $T^{2.8}$ electron-phonon scattering. (Bottom) Low-temperature portion of the same data, plotted on linear axes. The continuous curves show the best-fit contributions from e-e and T-independent dephasing terms.

where R_{xx} is the sheet resistance of the film, and the quantity $G = \frac{\pi\hbar}{e^2 R_{xx}}$. (We ignore an additional contribution[37] to $\tau_{i,(e-e)}^{-1}$ that is proportional to T^2, since it is smaller by a factor of $k_B T/E_F \sim 10^{-3}$.) At a temperature of 10 K, $\tau_{i,(e-e)}^{-1} \approx 10^{11}$ s^{-1}, or comparable to the e-p dephasing rate (calculated below) at this temperature. At lower temperatures, the dephasing field B_ϕ scales with R_{xx}^2 for samples 1 and 2; this is expected since both the dephasing rate and the inverse diffusion coefficient should be proportional to R_{xx}. We therefore use the above theory to estimate the diffusion coefficient, since the only parameters in Eq. (22) are the film sheet resistance and fundamental constants. For sample 1, we obtain 7.2 cm^2/s, comparable to the 4.05 cm^2/s estimated from the Drude scattering time. The temperature dependence of the e-e dephasing rate is plotted in Fig. 10 as a broken line and is the most significant contribution to the total rate at intermediate temperatures. This is consistent with the analysis of the resistance versus temperature data in Sec. III above, which showed dephasing linear in temperature between 1 and 10 K (i.e. a $\ln(T)$ prefactor indicating $p = 1$). We use the values for the diffusion coefficient extracted using the AAK theory D_{AAK} in the remainder of our analysis.

B. Electron-phonon scattering

There have been extensive measurements and analysis of e-p scattering contributions to dephasing in metallic and semiconducting thin films.[35] In particular, various theories have proposed, and some experiments have observed, T^2, T^3, and T^4 power-law dependencies of the scattering rate. For example, Lawrence and Meador[38] describe the e-p inelastic scattering rate $\tau_{i,(e-p)}^{-1}$ in a dirty 2D film:

$$\tau_{i,(e-p)}^{-1} = 14\pi\zeta(3)\lambda_{\mathrm{ep}}\omega_D\left(\frac{T}{\Theta_D}\right)^3, \tag{23}$$

where $\zeta(3)$ is the Riemann ζ function and ω_D and Θ_D are the Debye frequency and temperature. With $\Theta_D = 150$ K and $\lambda_{\mathrm{ep}} = 0.1$, at 10 K $\tau_{i,(e-p)}^{-1} \approx 10^{11}$ s^{-1}, comparable to the dephasing rate in Fig. 10. Other theories predict power laws in temperature with exponents between 2–4 for e-p scattering in a 2D film.

In addition to the above T-linear and T^x (with $x \sim 2$–4) contributions to the electron dephasing rate, spin-flip scattering from magnetic impurities (or several other intrinsic or extrinsic processes, see discussion in, e.g., Ref. 39) may lead to a temperature-independent contribution to the dephasing. We therefore fit the measured dephasing rates, plotted in Fig. 10, to the following form:

$$\tau_\phi^{-1} = \tau_\phi^{-1}(0) + C_{\mathrm{ee}}T + C_{\mathrm{ep}}T^x. \tag{24}$$

The zero-temperature rate $\tau_\phi^{-1}(0)$, and the T-linear coefficient C_{ee}, were obtained from fits to the data below 5 K, while the parameters x and C_{ep} for the e-p contribution were obtained using only the high temperature ($T > 10$ K) data. The resulting coefficients, along with other analysis results, are collected in Table III, and the individual contributions for sample 1 are shown as dotted curves in Fig. 10.

C. Dephasing in the $T \to 0$ limit

The lower panel of Fig. 10 plots the low-temperature dephasing rate data for all three samples along with the theoretical T-linear e-e dephasing and temperature independent contributions. In an ideal metallic film, e-e scattering should provide the only mechanism for electronic dephasing at low temperature, and so the rate should continue to decrease as the length scale over which interference effects occur increases. Any cutoff in this length scale, such as that due to finite sample size or another scattering mechanism, will lead to saturation of the dephasing rate or a temperature dependence that is weaker than the AAK T-linear theory. Such saturation or weak T dependence has been observed at low temperatures in many studies,[35] and various mechanisms have been considered. Typically, this effect is described by a temperature-independent contribution to the dephasing rate, $\tau_\phi^{-1}(0)$, although the physical relevance of such a description

TABLE III. Weak localization magnetoconductance analysis results. D_{tr} and D_{AAK} are the diffusion coefficient as determined from a free electron picture and by scaling the measured dephasing rate to the Al'tshuler-Aronov-Khmelnitski prediction (see text). B_e and B_{so} are the elastic and spin-orbit scattering transport fields and τ_{so} is the spin-orbit time. The parameters $\tau_\phi^{-1}(0)$, C_{ee}, C_{ep}, and x describe the temperature dependent dephasing rate [see Eq. (24) in the text.]

Parameter	Units	Sample 1	Sample 2	Sample 3
D_{tr}	cm^2/s	4.05	4.94	4.73
D_{AAK}	cm^2/s	7.0	10.1	11.1
B_e	T	20.0	12.6	11.1
$B_{so}^{\perp}$	T	0.81	0.69	1.94
$B_{so}^{\parallel}$	T	2.6	...	...
τ_{so}	10^{-13} s	2.9	2.36	0.76
$\tau_\phi^{-1}(0)$	10^9 s^{-1}	2.7	4.8	0
C_{ee}	10^{10} s^{-1}/K	1.18	1.01	0.70
C_{ep}	10^7 s^{-1}/K^x	5.9	17.3	10.5
x	...	2.78	2.56	2.78

in the limit of zero temperature may be unclear. Saturation effects may include both intrinsic mechanisms such as noise from two-level systems[40] or spin-flip scattering, and extrinsic ones, such as an ambient magnetic field, electron heating, or microwave noise effect.[41] Lin, Li, and Zhong[41] observed a systematic dependence of $\tau_\phi^{-1}(0)$ on D in disordered metals; based on this trend and with $D \approx 5$–10 cm^2/s the predicted saturation rate is $\approx 2 \times 10^{11}$–2×10^{12} s^{-1}, considerably higher than $\tau_\phi^{-1}(0) \sim 3$–4×10^9 s^{-1}. Recent studies of Sn-doped In_2O_{3-x} films[42] report a $\tau_\phi^{-1}(0)$ that decreases with increasing disorder, whereas sample 3 above (which has the smallest value of R_{xx}) shows no sign of a temperature independent dephasing contribution. The magnetic field corresponding to our $\tau_\phi^{-1}(0)$ is ~10 Gauss, and we estimate that residual fields within our cryostats are much less than this value. If the zero-temperature dephasing rate is due to spin-flip scattering, then this implies a magnetic impurity concentration of roughly 10 ppm[43] (see also the discussion in McGinnis and Chaikin[23]).

Finally, we comment on the departure from $\ln(T)$ behavior in our R_{xx} versus T data at the lowest temperatures, visible below 0.5 K in Fig. 3 for samples 1 and 2. A dephasing mechanism such as spin-flip scattering will suppress the QI correction but not affect the EEI contribution. In such a case the slope A would become larger since the QI and EEI $\ln(T)$ contributions are of opposite sign. However, we observe a downturn in the resistance (upturn in σ_{xx}) in the $T \to 0$ limit, suggesting that the electronic system itself is unable to cool effectively at these temperatures. Assuming that the $\ln(T)$ behavior does remain, we scaled the above scattering rates with "effective" values for the temperature assuming continued $\ln(T)$ behavior. While the tendency towards saturation becomes less pronounced after this scaling, the temperature dependence is still weaker than T linear, and we conclude that insufficient cooling is not responsible for the T-independent contribution to the dephasing $\tau_\phi^{-1}(0)$ in the above analysis.

VII. SUMMARY AND CONCLUSIONS

Our analysis has shown that even the most metallic phase-change films studied here are governed by strong defect scattering and hence qualify as "dirty metals," with a rich physics of QI and EEI effects. Significantly, in these materials we have a simple way of tuning the disorder without changing composition. This provides an excellent opportunity to study systematic trends as a function of increasing disorder. By analyzing three samples with different room-temperature sheet resistances, we are able to study disorder and thickness dependence and anisotropy of spin-orbit scattering, strengthening of the e-p scattering rate with increasing disorder, and suggestions of a sub-T-linear power law governing electronic dephasing in the low-temperature limit. Our preliminary analysis of even more disordered films reveals a departure from $\ln(T)$ behavior and apparent saturation of the resistance at low temperature; we will address this crossover to the strongly localized regime in future work.

We have studied the low-temperature magnetotransport properties of disordered thin films of the phase-change compound $GeSb_2Te_4$ that have been annealed to be weakly metallic. We observe clear signatures of WAL and disorder-enhanced EEI effects in the resistivity, magnetoconductance, and Hall effect measurements. Using established WL theory, we are able to extract several important materials parameters, including characteristic spin-orbit and inelastic scattering rates. We observe a $\ln(T)$ quantum correction in R_H 1.4 times larger than that seen in R_{xx}, comparable to the factor of two expected when the QI effects are suppressed at high field. Extracted spin-orbit scattering rates are consistent with the EY mechanism for spin relaxation. The inelastic scattering is dominated by phonons at high temperatures, e-e scattering at low temperature, and shows a weak temperature dependence at the lowest temperatures studied. We have examined the existence of saturation or a cutoff in the dephasing length at very low temperature, which could arise from either intrinsic (spin-flip scattering due to magnetic impurities) or extrinsic (coupling to external dissipative phenomena) sources. Further study of dephasing mechanisms in ultrathin GST films should prove to be relevant to open questions about the nature of metallic behavior in low-dimensional disordered systems.

ACKNOWLEDGMENTS

This work was supported by the National Science Foundation grant NSF-DMR-9508419, FENA, as well as the German Science Foundation (DFG), within the SFB 917 ("Nanoswitches"). We acknowledge many useful discussions with Boris Spivak, Peter Jost, Li Zhang, Ko Munakata, and George Karakonstantakis.

[1]M. Wuttig and N. Yamada, Nat. Mater. **6**, 824 (2007).
[2]I. Friedrich, V. Weidenhof, W. Njoroge, P. Franz, and M. Wuttig, J. Appl. Phys. **87**, 4130 (2000).
[3]G. Bruns, P. Merkelbach, C. Schlockermann, M. Salinga, M. Wuttig, T. D. Happ, J. B. Philipp, and M. Kund, Appl. Phys. Lett. **95**, 043108 (2009).
[4]D. Loke, T. H. Lee, W. J. Wang, L. P. Shi, R. Zhao, Y. C. Yeo, T. C. Chong, and S. R. Elliott, Science **22**, 1566 (2012).
[5]T. Siegrist, P. Jost, H. Volker, M. Woda, P. Merkelbach, C. Schlockermann, and M. Wuttig, Nat. Mater. **10**, 202 (2011).
[6]P. A. Lee and V. Ramakrishnan, Rev. Mod. Phys. **57**, 287 (1985).
[7]See, for example, G. Bergmann, Phys. Rep. **107**, 1 (1984); B. L. Altshuler, A. G. Aronov, M. E. Gershenson, and Yu. V. Sharvin, Sov. Sci. Rev. A. Phys. **9**, 223 (1987).
[8]F. V. Tikhonenko, A. A. Kozikov, A. K. Savchenko, and R. V. Gorbachev, Phys. Rev. Lett. **103**, 226801 (2009).
[9]A. D. Caviglia, M. Gabay, S. Gariglio, N. Reyren, C. Cancellieri, and J. M. Triscone, Phys. Rev. Lett. **104**, 126803 (2010).
[10]F. J. Wong, R. V. Chopdekar, and Y. Suzuki, Phys. Rev. B **82**, 165413 (2010).
[11]J. Wang, A. M. DaSilva, C.-Z. Chang, K. He, J. K. Jain, N. Samarth, X.-C. Ma, Q.-K. Xue, and M. H. W. Chan, Phys. Rev. B **83**, 245438 (2011).
[12]J. Chen, X. Y. He, K. H. Wu, Z. Q. Ji, L. Lu, J. R. Shi, J. H. Smet, and Y. Q. Li, Phys. Rev. B **83**, 241304 (2011).
[13]B. S. Lee, J. R. Abelson, S. G. Bishop, D. H. Kang, B. Cheong, and K. B. Kim, J. Appl. Phys. **97**, 093509 (2005).
[14]S. T. Lim, L. Hui, J. F. Bi, and K. L. Teo, J. Appl. Phys. **110**, 113916 (2011).
[15]J. Kim, J. Kim, and S. H. Jhi, Phys. Rev. B **82**, 201312 (2010).
[16]M. Xu, Y. Q. Cheng, L. Wang, H. W. Sheng, Y. Meng, W. G. Yang, X. D. Han, and E. Ma, Proc. Natl. Acad. Sci. USA **109**, E1055 (2012).
[17]J. Tominaga, R. E. Simpson, P. Fons, and A. V. Kolobov, Appl. Phys. Lett. **99**, 152105 (2011).
[18]Z. Sun, Y. Pan, J. Zhou, B. Sa, and R. Ahuja, Phys. Rev. B **83**, 113201 (2011).
[19]J. M. Ziman, *Electrons and Phonons* (Oxford University Press, Oxford, 1960).
[20]P. Zalden, C. Bichara, J. v. Eijk, R. P. Hermann, I. Sergueev, G. Bruns, S. Buller, W. Bensch, T. Matsunaga, N. Yamada, and M. Wuttig, Mater. Res. Soc. Symp. Proc. **1338**, mrss11-1338-r06-03 (2011).
[21]S. Hikami, A. I. Larkin, and Y. Nagaoka, Prog. Theor. Phys. **63**, 707 (1980).
[22]B. L. Al'tshuler and A. G. Aronov, Solid State Commun. **46**, 429 (1983).
[23]W. C. McGinnis and P. M. Chaikin, Phys. Rev. B **32**, 6319 (1985).
[24]H. Fukuyama, J. Phys. Soc. Jpn. **49**, 644 (1980); B. L. Altshuler, D. Khmel'nitzkii, A. I. Larkin, and P. A. Lee, Phys. Rev. B **22**, 5142 (1980); H. Fukuyama, J. Phys. Soc. Jpn. **52**, 18 (1983).
[25]D. J. Bishop, D. C. Tsui, and R. C. Dynes, Phys. Rev. Lett. **46**, 360 (1981); M. J. Uren, R. A. Davies, and M. Pepper, J. Phys. C **13**, L985 (1980).
[26]B. Shinozaki, K. Makise, Y. Shimane, H. Nakamura, and K. Inoue, J. Phys. Soc. Jpn. **76**, 074718 (2007).
[27]B. L. Altshuler and A. G. Aronov, Zh. Eksp. Teor. Fiz. Pis'ma Red. **33**, 515 (1981) [JETP Lett. **33**, 499 (1981)].
[28]M. E. Gershenzon, B. N. Gubankov, and Yu. E. Zhuravlev, Zh. Eksp. Teor. Fiz. **83**, 2348 (1982) [Sov. Phys. JETP **56**, 1362 (1982)].
[29]R. Rosenbaum, Phys. Rev. B **32**, 2190 (1985).
[30]A. A. Abrikosov and L. P. Gor'kov, Zh. Eksp. Teor. Fiz. **42**, 1088 (1962) [Sov. Phys. JETP **15**, 752 (1962)]; R. Meservey and P. M. Tedrow, Phys. Rev. Lett. **41**, 805 (1978).
[31]P. G. Elliott, Phys. Rev. **96**, 266 (1954); Y. Yafet, *Solid State Physics* (Academic, New York, 1963).
[32]R. L. Kallaher and J. J. Heremans, Phys. Rev. B **79**, 075322 (2009).
[33]S. Sangiao, N. Marcano, J. Fan, L. Morellón, M. R. Ibarra, and J. M. de Teresa, Europhys. Lett. **95**, 37002 (2011).
[34]M. Eshkol, E. Eisenberg, M. Karpovski, and A. Palevski, Phys. Rev. B **73**, 115318 (2006).
[35]J. J. Lin and J. P. Bird, J. Phys.: Condens. Matter. **14**, R501 (2002).
[36]B. L. Al'tshuler, A. G. Aronov, and D. E. Khmelnitsky, J. Phys. C **15**, 7367 (1982).
[37]B. N. Narozhny, G. Zala, and I. L. Aleiner, Phys. Rev. B **65**, 180202 (2002).
[38]W. E. Lawrence and A. B. Meador, Phys. Rev. B **18**, 1154 (1978).
[39]Y. Imry, *Introduction to Mesoscopic Physics*, 2nd ed. (Oxford University Press, Oxford, 2002).
[40]Y. Imry, H. Fukuyama, and P. Schwab, Europhys. Lett. **47**, 608 (1999).
[41]J. J. Lin, T. J. Li, and Y. L. Zhong, J. Phys. Soc. Jpn. **72**, 7 (2003).
[42]C. Y. Wu, B. T. Lin, Y. J. Zhang, Z. Q. Li, and J. J. Lin, Phys. Rev. B **85**, 104204 (2012).
[43]D. Davidov, C. Rettori, R. Orbach, A. Dixon, and E. P. Chock, Phys. Rev. B **11**, 3546 (1975).